NSRRC -J05139 (2016)

FULL PAPER

ADVANCED FUNCTIONAL MATERIALS
www.afm-journal.de

Materials Views
www.MaterialsViews.com

# The Novel Additive 1-Naphthalenethiol Opens a New Processing Route to Efficiency-Enhanced Polymer Solar Cells

*Hong-Jyun Jhuo, Sih-Hao Liao, Yi-Lun Li, Po-Nan Yeh, Show-An Chen,* Wei-Ru Wu, Chun-Jen Su, Jey-Jau Lee, Norifumi L. Yamada, and U-Ser Jeng**

**Polymer solar cells (PSCs) based on fullerene derivatives often require additives to optimize active layer morphology. Here, the novel additive 1-naphthalenethiol (SH-na) is proposed for processing the PSC active layer of PTB7:$PC_{71}BM$. Spin-casting with SH-na as additive achieves a power conversion efficiency (PCE) of 7.3%, compared to 6.7% for preparations containing the conventional 1,8-diiodooctane additive. Dipping of the active layer into a methanol solution of critical SH-na concentration increases the PCE further to 8.75%. This is mainly due to an improved open-circuit voltage (from 0.72 to 0.79 V) together with a high achieved fill factor of 0.70. The improved PCE is correlated to the morphology optimization according to measurements of grazing incidence small/wide-angle X-ray scattering, neutron reflectivity, atomic force microscopy, Fourier transform infrared spectroscopy, and X-ray photoelectron spectroscopy. The integrated results suggest that the halogen-free additive SH-na can form hydrogen bonds with both PTB7 and $PC_{71}BM$, resulting in substantially improved PTB7 crystallization and multi-length-scale $PC_{71}BM$ dispersion for appropriate aggregation and networks. The subsequent dipping treatment with SH-na further modifies the active layer morphology for a more $PC_{71}BM$-enriched surface and better $PC_{71}BM$ networks in the bulk film for an optimized electron-to-hole mobility ratio of 2.04, hence resulting in improved device performance.**

## 1. Introduction

Bulk heterojunction (BHJ) polymer solar cell (PSC) is regarded as one of the promising renewable energy resources with the advantages of low cost, flexible devices, and solution processing for large area.[1] Device performance of PSCs has been improved greatly via molecular design and device structure architecture in the past few years. Blending the representative middle-bandgap poly-3-hexylthiophene (P3HT) with an acceptor indene-C60-Bisadduct of a higher lowest unoccupied molecular orbital level fullerene led to a high power conversion efficiency (PCE) over 7%.[2,3] Low bandgap polymers were used to extend light absorption for better short-circuit current ($J_{sc}$) and open-circuit voltage ($V_{oc}$) through modulated highest occupied molecular orbital level, hence further enhanced PCE. Among low bandgap polymers, fluorinated-thieno[3,4-b]thiophene-based PTB7 is one of the most widely used materials in the PSCs with high PCE. For examples, with improved crystallinity of PTB7[4] and enhanced light absorption with embedded nanoparticles via plasmon resonance in a PTB7:$PC_{71}BM$ system, the PCE value could reach 8%.[5] Recently, over 10% PCE was achieved using an active layer of the low bandgap polymer PTB7-Th along with dual-doped (indium and fullerene derivatives) ZnO as the cathode interlayer.[6] Comparably impressive PCE was also demonstrated with the homologous low-bandgap polymers of PffBT4T-2OD with either $TC_{71}BM$ or several other fullerene derivatives via morphology optimization.[7] These achievements renew the interest in developing PSCs and the relevant morphology control after the discovery of highly efficient but lead-containing perovskite solar cells.[8]

Morphology control of the PSC active layer includes thermal annealing,[9] solvent annealing,[10] adding additive,[11–17] and surface modification.[18,19] For PSCs with high PCE, adding additive into the solution of the active layer blends for spin-coating has been generally adopted as an indispensable strategy for film morphological control. For examples, alkyl additive such as 1,8-octanedithiol (ODT) was demonstrated to effectively

H.-J. Jhuo, Dr. S.-H. Liao, Y.-L. Li, P.-N. Yeh, Prof. S.-A. Chen
Chemical Engineering Department and Frontier Research Center on Fundamental and Applied Sciences of Matters
National Tsing-Hua University
Hsinchu, 30013 Taiwan, Republic of China
E-mail: sachen@che.nthu.edu.tw
W.-R. Wu, Dr. C.-J. Su, Dr. J.-J. Lee, Prof. U. Jeng
National Synchrotron Radiation Research Center
No. 101, Hsin-An Road, Hsinchu, 30077 Taiwan, Republic of China
E-mail: usjeng@nsrrc.org.tw
Prof. U. Jeng
Chemical Engineering Department
National Tsing-Hua University
Hsinchu, 30013 Taiwan, Republic of China
Prof. N. L. Yamada
Neutron Science Laboratory
High Energy Accelerator Research Organization
Tokai, Naka 319-1106, Japan

DOI: 10.1002/adfm.201505249


© 2016 WILEY-VCH Verlag GmbH & Co. KGaA, Weinheim

redshift light absorption and increase the crystallinity of PCPDTBT,[11] resulting in an improved PCE from 2.8% to 5.5%.[12] ODT with two thiol groups was also found to improve the crystallinity and hole mobility in conventional P3HT:$PC_{61}BM$ system.[13] The most widely used 1,8-diiodooctane (DIO) could effectively suppress large aggregation of $PC_{71}BM$, thereby promoting drastically the device PCE of PTB7:$PC_{71}BM$ system from 3.92% to 7.40%.[14]

In addition to alkyl additives, several planar and rigid molecules have been used for PSCs. For examples, 3-methylthiophene was found to increase the crystallinity of P3HT and enhanced PCE of the P3HT:$IC_{70}BA$ system from 5.80% to 6.69%.[15] The 1-chloronaphthalene additive could prevent $IC_{70}BA$ from large-scale aggregation while retaining nanoscale phase separation,[2,16] resulting in a leap in efficiency from 4.12% to 7.40%.[2] With 1-methylnaphthalene additive, the copolymer (PIDT-phanQ) blend with $PC_{71}BM$ also alleviated its large $PC_{71}BM$ cluster aggregation for a dramatically improved PCE from 0.03% to 6.1%.[17a] In contrast to bulk modulation of the active layer of PSCs, surface modification with polar non-solvents was shown to further improve the PCE of the PTB7:$PC_{71}BM$ system from 7.10% to 7.94%,[18,19] owing to reduction of surface traps for increased electron density near the surface of the active layer.

In this study, we propose a new additive 1-naphthalenethiol (SH-na) that can serve for integrated bulk and surface morphology controls, via a conventional spin-casting process followed by a novel SH-na solution dipping treatment. We demonstrate that the hence obtained device with PTB7:$PC_{71}BM$ blend can reach 8.75% PCE, which is superior to 6.73% obtained for the same system prepared with a conventional processing with DIO additive. Recently, a postadditive soaking process was proposed to modify the morphology by dripping mixed non-solvent (cyclohexane/n-hexane with a small fraction of DIO) on an active layer followed with spin-casting, which resulted in PCE improvement of PTB7:$PC_{71}BM$ system from 3.86% to 8.14%.[20] In our case, the use of the halogen-free SH-na additive in spin-casting followed by additive solution dipping is of variated mechanism for different morphological features, as revealed from the integrated structural information obtained from the decisive processing stages.[20] SH-na has some unpleasant odor similar to mercaptan and is normally stored under nitrogen atmosphere. Its odor will not retain in the device as it is added in small quality and will be removed by vacuum pumping during the device fabrication process. Its boiling point is (285 °C) higher than the solvent chlorobenzene (CB; 131 °C). In contrast to the DIO additives with selected affinity toward fullerene derivatives,[12a] SH-na has a planar, rigid molecular structure, and a thiol group that can form hydrogen bonds with both PTB7 and $PC_{71}BM$. Thereby, SH-na facilitates both PTB7 crystallization and multi-length-scale $PC_{71}BM$ dispersion during the film spin-coating process. Furthermore, SH-na can modify the surface composition significantly during the subsequent dipping treatment. The hence modulated morphological features are correlated to the enhanced hole and electron mobility of the devices, to illustrate the underlying mechanism of the new PSC processing proposed.

We note that there is an increasing interest in developing large-area roll-to-roll processing for PSCs.[17b] The PCE values of roll-to-roll fabricated devices are generally inferior to that processed using solution spin-casting. The solution-dipping methodology developed here is suitable for large-area processing, and may be potentially used as a post-treatment of roll-to-roll processing to achieve large area devices with improved PCE values. In addition, the halogen-free additive SH-na proposed here is not only more efficient in PCE improvement but also relatively more environmental friendly in mass-production of PSCs as compared to the often used DIO additive.

## 2. Results and Discussion

### 2.1. SH-na Effects on Device Performance

**Figure 1** illustrates the chemical structures of PTB7 and $PC_{71}BM$, the additives DIO and SH-na, and the new processing route of the PSC proposed. Shown in **Table 1** are the performances of the PTB7:$PC_{71}BM$ devices prepared from spin-casting the blend solutions of CB containing 25 mg $mL^{-1}$ of PTB7:$PC_{71}BM$ (blend ratio 1:1.5 by weight) with or without 3 vol% additive (SH-na or DIO). Note that 3 vol% SH-na in the spin cast sample solution is the optimal concentration for the devices (as illustrated in Table S1 in the Supporting Information). Also shown are the device performances for that further subject to a dipping treatment: by dipping the active layers in a methanol solution containing 4.5% SH-na for three seconds followed by spinning off residual solution, in which the dipping time (Figure S1 and Table S2, Supporting Information) and SH-na concentration (Table S3, Supporting Information) of dipping treatment is optimal for the devices. All the devices were fabricated with the conventional configuration of ITO/PEDOT:PSS/PTB7:$PC_{71}BM$/Ca/Al. The device with the active layer spin-cast from the CB solution of 3 vol% SH-na additive showed much improved $V_{oc}$ (0.78 V), leading to a higher PCE of 7.30% than that of the device prepared with DIO (6.73%) and that of the device prepared without any additive (3.99%). The PCE improvement of the devices processed with the SH-na additive is mainly attributed to the significantly promoted $V_{oc}$, which is the highest among the reported values for the systems based on the PTB7 blend with fullerene derivatives.[21] Moreover, with the active layer (spin-cast with 3 vol% SH-na in CB) subject to the dipping treatment (4.5 vol% SH-na in methanol), the PCE increases from 7.30% to 8.75%; such improvement is attributed to the reduced series resistance and increased shunt resistance for hence the increased $J_{sc}$ and FF values (Table 1). In addition, the corresponding external quantum efficiency (EQE) measurements illustrate an overall improvement in the wavelength range from 300 to 800 nm (**Figure 2**b); the integrated $J_{sc}$ is consistent with $J$–$V$ measurement within 3% error (Figure 2a). The obtained PCE of 8.75% is an impressively high value among the conventional type PSCs with PTB7, and is comparable to the literature value 8.92% of the PTB7:$PC_{71}BM$ system embedded with Au-core/Si-shell nanoparticles for additional plasmonic effects.[5] Our result proves that the simple strategy of morphology refinement using SH-na additive followed by the SH-na/methanol solution dipping for morphology optimization could reach comparable PCE to the previous case of elaborately included plasmonic effects.


© 2016 WILEY-VCH Verlag GmbH & Co. KGaA, Weinheim

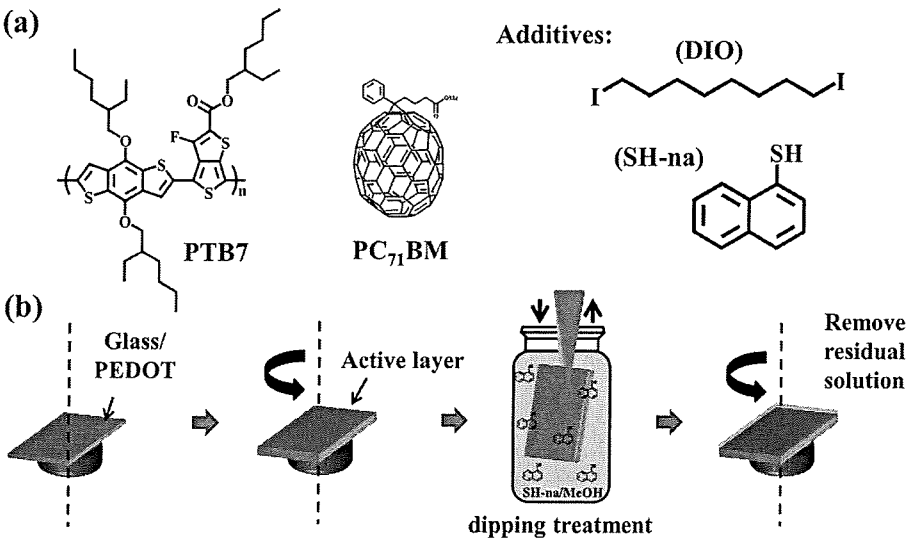


**Figure 1.** a) Chemical structures of the materials used for b) the device processing with spin-casting of the active layer followed by the dipping treatment illustrated.

Interestingly, we also found that the active layer processed without any additive dipping into a methanol solution containing a critically optimized 4.5 vol% SH-na (Table S3, Supporting Information) could also result in a dramatic PCE increase from 3.99% to 8.35%. The corresponding improved $V_{oc}$, $J_{sc}$, and FF values were summarized in Table 1. Presumably, given the critical SH-na concentration in the methanol dipping solution, the additive could quickly diffuse and distribute evenly into the just-cast film, and efficiently refine the surface composition, as revealed in the structural characterization below.

### 2.2. Tracing the Additive during Processing with Infrared and UV–vis Absorption

The associations of SH-na with PTB7 and $PC_{71}BM$ through hydrogen bonding were revealed using Fourier transform infrared spectroscopy (FT-IR). The FT-IR spectra (**Figure 3a**) for the neat PTB7 thin films (on KBr plates) spin-cast from the CB solution with 3 vol% SH-na additive exhibited two characteristic absorption peaks (1700 and 1720 $cm^{-1}$) of the carbonyl group (resulted from *cis* and *trans* configurations of the thienothiophene subunit, respectively),[23] which were shifted from those (1705 and 1725 $cm^{-1}$) observed for the film processed without SH-na by 5 $cm^{-1}$ each. For the $PC_{71}BM$ film, a similar shifting of the carbonyl group absorption peak from 1735 to 1730 $cm^{-1}$ also by 5 $cm^{-1}$ was also observed (Figure 3a) for the $PC_{71}BM$ film due to the presence of SH-na of a signature thiol-group absorption peak at 2570 $cm^{-1}$ (Figure S2, Supporting Information). These results indicate clearly that SH-na could form hydrogen bonding with both PTB7 and $PC_{71}BM$.[24]

We emphasize the necessity of using the two-step processing (spin-casting the blend solution with SH-na additive followed by SH-na/methanol solution dipping) in achieving the best PCE performance of 8.75%. Increasing the SH-na content over 3 vol% in the blend solution for spin-casting or solely dipping treatment of the spin-cast film (processed without additive) could not reach this high PCE value (Table S1, Supporting Information). These results imply that sequential modification of the bulk and surface film morphological features with the two-step processing is critical. With the IR absorption peak of the characteristic thiol vibration of SH-na (Figures S3 and S4 and Table S4, Supporting Information), we have traced SH-na content in the film immediately after spin-casting (via the IR absorption of the thiol group at 2570 $cm^{-1}$), and found significant residual SH-na in the just-cast active layer. Moreover, the absorption peak intensity of SH-na was found to enhance with

**Table 1.** Photovoltaic performance based on a conventional device structure of ITO/PEDOT:PSS/PTB7:$PC_{71}BM$ (80 nm)/Ca (5 nm)/Al (100 nm).

| Additive | Dipping | $V_{oc}$ [V] | $J_{sc}$ [mA $cm^{-2}$] | FF | PCE[a)] [%] | $PCE^{best}$ [%] | $R_s$[b)] [Ω $cm^2$] | $R_{sh}$[c)] [Ω $cm^2$] |
|---|---|---|---|---|---|---|---|---|
| Without | – | 0.70 ± 0.005 | 11.43 ± 0.23 | 0.46 ± 0.025 | 3.68 ± 0.31 | 3.99 | 11.57 | 221 |
| DIO | – | 0.72 ± 0.005 | 14.36 ± 0.10 | 0.64 ± 0.008 | 6.62 ± 0.11 | 6.73 | 4.24 | 556 |
| SH-na | – | 0.78 ± 0.005 | 13.97 ± 0.14 | 0.66 ± 0.003 | 7.19 ± 0.11 | 7.30 | 5.46 | 579 |
| Without | Yes | 0.79 ± 0.005 | 15.51 ± 0.17 | 0.67 ± 0.004 | 8.21 ± 0.14 | 8.35 | 3.83 | 604 |
| SH-na | Yes | 0.79 ± 0.005 | 15.67 ± 0.19 | 0.70 ± 0.018 | 8.42 ± 0.33 | 8.75 | 3.51 | 793 |

[a)]Device performance parameters are averaged from that of five devices, with the best PCE values listed; [b)]$R_s$, calculated from the inverse slope of *J–V* curve under illumination at $J = 0$[22]; [c)]$R_{sh}$, calculated from the inverse slope of *J–V* curve under illumination at $V = 0$.[22]


© 2016 WILEY-VCH Verlag GmbH & Co. KGaA, Weinheim

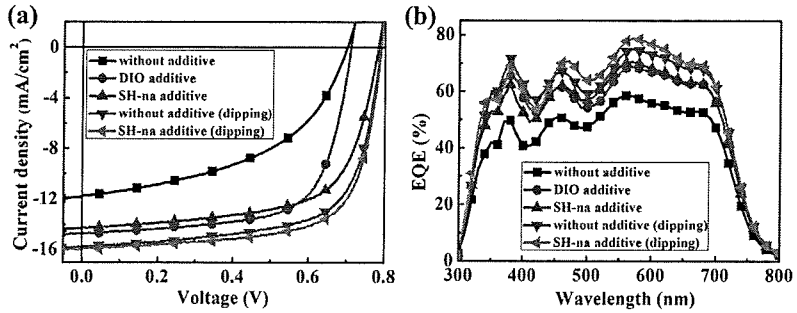


**Figure 2.** a) *J–V* curves of the PTB7:$PC_{71}BM$ devices processed with the different routes indicated. b) The corresponding EQE measurements.

the increase of the SH-na content (from 2 to 6 vol%) used in the blend solutions of CB for spin-casting. The SH-na residual concentration of the just-cast film could be further modulated by the dipping process with a solution containing SH-na. Specifically, tuning the SH-na concentration in a methanol dipping solution above a critical SH-na concentration of 4.0 vol% could change the dipping process from an additive-extraction to additive-enriching for the additive content in the just-cast PTB7:$PC_{71}BM$ (with 3 vol% SH-na additive) film as shown in Table S4 (Supporting Information). With 4.5% SH-na in the dipping solution, the best PCE value was achieved (shown in Table S3, Supporting Information). In contrast, a pure methanol dipping solution without additive could quickly and completely remove the residual SH-na additive from the just-cast PTB7:$PC_{71}BM$ film as evidenced from the disappearance of the characteristic IR absorption of SH-na (Figure S3b, Supporting Information). Residual SH-na in all the active layers could be removed completely under a high vacuum ($2 \times 10^{-6}$ torr) environment for 1 h before thermal deposition of the metal cathode; such process is similar to that for removal of DIO from the DIO-processed active layers (shown in Figure S4 and Table S4, Supporting Information).[25]

UV–vis absorption spectroscopy (Figure 3b) was used to determine the absorbance of PTB7:$PC_{71}BM$ prepared with the additives (DIO and SH-na) and the effect of the dipping treatment with SH-na in methanol. The absorbance of PTB7 mainly located in a longer wavelength region (500–750 nm), while that of $PC_{71}BM$ mainly located in a relatively shorter wavelength region (300–500 nm).[26,27] For the active layers processed with SH-na additive and/or dipping treatment, the absorption at 680 nm increased, which is correlated to enhanced PTB7 chain alignment[28] and thus improved crystallinity, as also revealed from the X-ray scattering results shown below.

### 2.3. Morphological Features Revealed with X-Ray Scattering

The PCE performance of BHJ PSCs critically depends on morphological controls to form bicontinuous/interpenetrating networks of the polymer and fullerene-derivative domains in the active layers. The crystallinity of the polymer affects not only the hole transport behavior but also the miscibility with fullerene derivatives, and hence the morphology of the resultant active/ layer.[29] Crystallization of PTB7 and aggregation of $PC_{71}BM$ in the active layers of different processing routes (with SH-na, DIO, and/or the dipping treatment) were investigated here with grazing incidence wide- and small-angle X-ray scattering (GIWAXS and GISAXS). The GIWAXS patterns shown in Figure S5 (Supporting Information) reveal the characteristic (100) peak of PTB7 crystallites and the short-range ordering peak of $PC_{71}BM$ aggregates in the blend film. Moreover, the isotropic broad (100) halo of PTB7 implies randomly oriented small crystalline grains in these films.[4] These GIWAXS profiles were extracted respectively along the in-plane ($q_y$) (**Figure** 4a) and out-of-plane ($q_z$) (Figure S6, Supporting Information) from the corresponding 2D GIWAXS patterns, revealing a marginally preferred face-on orientation of PTB7 crystallites (Figure S6, Supporting Information); which may be beneficial for enhancing vertical hole transport and thus improved device performance.[23] The PTB7 (100) reflections (corresponding to ordered packing along the polymer side-chains) for the active layers processed without additive, with DIO, and with SH-na, locate respectively at the scattering vector $q = 0.351$, 0.357, and 0.355 Å$^{-1}$ (with $q = 4\pi\lambda^{-1} \sin\theta$ defined by the X-ray wavelength $\lambda$ and scattering angle $2\theta$), corresponding to characteristic layer spacings of 17.9, 17.6, and 17.7 Å, respectively. The result suggests that the additives could facilitate tightening of the chain

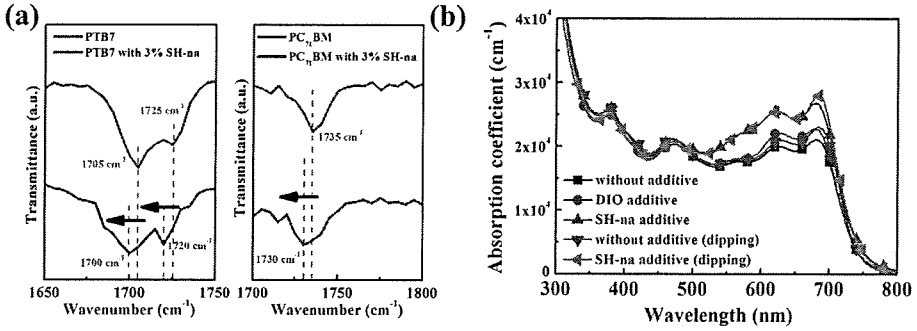


**Figure 3.** a) FT-IR spectra of the carbonyl group absorption bands of neat PTB7 (left) and $PC_{71}BM$ (right) thin films, spin-cast from CB solutions with or without 3 vol% SH-na as indicated. The arrows mark the shifting of the characteristic absorption peaks at the presence of SH-na. b) UV–vis absorption spectra of the PTB7:$PC_{71}BM$ thin films processed with the different routes indicated.


© 2016 WILEY-VCH Verlag GmbH & Co. KGaA, Weinheim

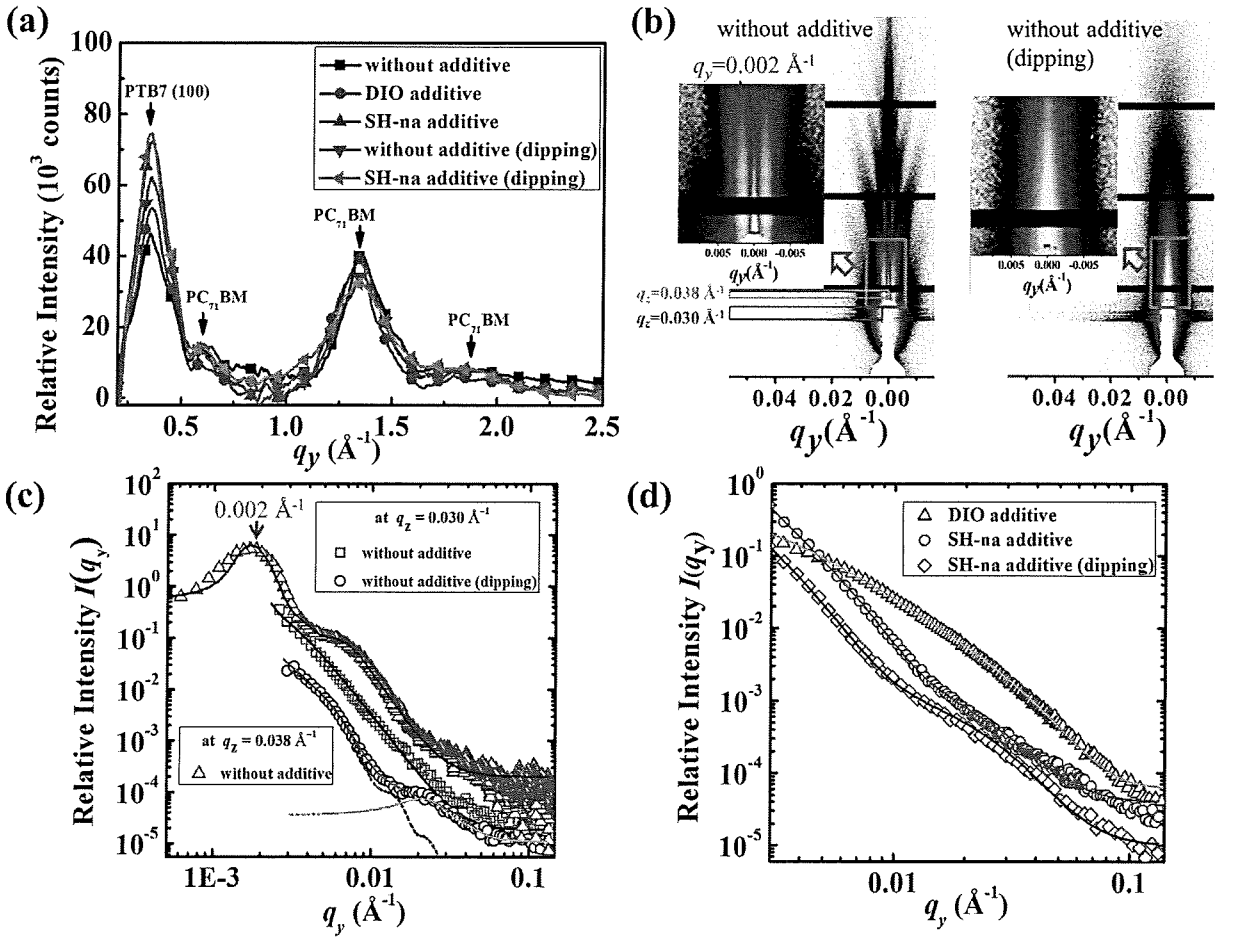


**Figure 4.** (AU to ATP: Enlarge the figures by 50%,via cross-column style, for important data/fitting details) a) GIWAXS in-plane profiles extracted from the corresponding 2D patterns of the active layers of PTB7:$PC_{71}BM$ prepared with the different routes as indicated. The characteristic PTB7 (100) and $PC_{71}BM$ ordering peaks are marked by arrows. b) 2D GISAXS patterns of the active layers processed without additive and that subjected to the dipping treatment. The much richer scattering features marked by the square (with the eminent scattering strips highlighted with an arrow in the inset; left) correspond to in-plane phase-separated and ordered domains of the film processed without additive; these scattering features are largely eliminated after the dipping treatment (GISAXS pattern to the right-hand-side). c) Corresponding in-plane GISAXS profiles extracted at $q_z = 0.03$ Å$^{-1}$ are fitted (solid curves) respectively with the models described in the text. The dotted thick blue and thin green curves describe the scattering contributions from large and small $PC_{71}BM$ aggregates, respectively. An additional profile is extracted at higher $q_z = 0.038$ Å$^{-1}$ and fitted for the in-plane ordering peak at $q_y = 0.002$ Å$^{-1}$, as also marked in panel (b). d) Model-fitted GISAXS profiles extracted at $q_z = 0.030$ Å$^{-1}$ for the PTB7:$PC_{71}BM$ active layers processed with the different routes indicated. Fitting models and fitted parameters are summarized in Table 2.

packing of PTB7; which is consistent with the previous UV–vis absorption result mentioned.[13b] Moreover, the integrated (100) peak intensity in Figure 4a (proportional to crystallinity) of the active layer prepared with SH-na and DIO additive are significantly higher than that prepared without additive by the factor 2.0 and 1.3, respectively (Table S5, Supporting Information). For the active layers prepared without additive after dipping treatment, the (100) peak also significantly enhanced by a factor 1.56, implying the dipping treatment can substantially improve crystallinity of PTB7.

The GIWAXS profiles of the blend films in Figure 4a also exhibit the same ordering peaks of $PC_{71}BM$ aggregates of pure $PC_{71}BM$ spin-cast film at $q \approx 0.65$, 1.33, and 1.86 Å$^{-1}$,[23] revealing a similar local packing structure in these films from the different routes. In contrast, the GISAXS 2D patterns (Figure 4b) and 1D in-plane profiles (Figure 4c) show distinct features in the observed $q$-range. Accumulated studies already established that GISAXS scattering features were largely dominated by PCBM-aggregates in the PCBM-based PSC active layers.[30,31] The GISAXS 2D patterns of the active layer without additive exhibit much richer scattering features than those by other processing routes (Figure 4b and Figure S7 in the Supporting Information) with the several oblique side peaks oriented with ≈10° away from the surface normal direction; these features correspond to faceted surface morphology of the active layer processed without additive, as suggested in previous reports.[32] The most distinct feature in all the GISAXS patterns is the strong vertical scattering stripes located near $q_y \approx 0.002$ Å$^{-1}$ (marked with green square in Figure 4b) uniquely observed with the active layer prepared without additive. Such


© 2016 WILEY-VCH Verlag GmbH & Co. KGaA, Weinheim

scattering feature indicates existence of phase-separated $PC_{71}BM$-rich domains with a large mean spacing ($d$) ≈314 nm (as estimated from the scattering peak position $q_y$ using the Bragg law $d = 2\pi/q_y$) along the in-plane direction of the film.[32] These in-plane phase-separated domains are further evidenced with the corresponding atomic force microscopy (AFM) image shown below. Comparably large phase-separated $PC_{71}BM$ domains from spin-cast PTB7:$PC_{71}BM$ (processed without additive) films were reported previously.[33] In contrast, all the other GISAXS patterns (Figure S7, Supporting Information) for the active layers prepared with additive and/or dipping treatment, exhibit little or no such scattering strips in the low-$q_y$ region (0.001–0.003 $Å^{-1}$), implying that the large phase-separated $PC_{71}BM$-rich domains could be largely eliminated by the additive (DIO or SH-na) during spin-casting[14–17,31] or by the SH-na additive solution dipping treatment.

To gain more structural information of the $PC_{71}BM$ aggregates in the active layers, we further analyze the GISAXS profiles $I(q_y)$ extracted at the specular beam position within the region $q_z = 0.03 \pm 0.002$ $Å^{-1}$ (as marked in Figure S7 in the Supporting Information), and along in-plane direction of the 2D patterns mainly for better intensity (as that done in previous reports[30,31]. Shown in Figure 4c are the characteristically different in-plane GISAXS profiles for the active layers without additive and that subject to the methanol/SH-na solution dipping treatment. Based on the dimensions of the large spherical domains observed from AFM (**Figure 5**a), the former GISAXS profile can be best-fitted with ellipsoidal aggregates (cf. the ellipsoid model detailed in the Supporting Information) with major and minor axes of $2A = 14 \pm 4$ nm and $2B = 260 \pm 26$ nm (Figure 4c) with the a size polydispersity ($P$, 0% < $P$ < 100%, $P$ = 0%: monodisperse) of 40% (assuming a Schultz distribution as detailed in Figure S7 in the Supporting Information).[34] Note that the large dimension 260 nm of the oblate aggregates (with $2A << 2B$) is modeled to be oriented preferentially along the in-plane direction. An additional in-plane profile $I(q_y)$ is also extracted at higher $q_z = 0.038$ $Å^{-1}$ (circumventing the beamstop-blocked scattering zone, marked with blue square as shown in Figure 4b) to illustrate the interference peak at $q_y \approx 0.002$ $Å^{-1}$; the profile could be adequately fitted (Figure 4c) with the same size of oblate aggregates of a mean in-plane spacing of 312 nm (assuming a structure factor of hard-sphere interactions). All the GISAXS fitting parameters are summarized in **Table 2** and the corresponding fitting models are detailed in the Supporting Information. In contrast, the GISAXS profile for the active layer subject to the dipping treatment could be best-fitted (Figure 4c) by the bimodal size distributions (ellipsoid and sphere aggregates models, as shown in red solid line in Figure 4c), which comprising smaller prolate aggregates (with $2A = 183$ nm along the in-plane direction and $2B = 20$ nm, fitted with blue bold dash line in Figure 4c) and small globular $PC_{71}BM$ aggregates (of a mean diameter of 10 nm with the polydispersity of 27%, fitted with green thin dash line in Figure 4c) to account for the scattering hump at $q_y \approx 0.025$ $Å^{-1}$. Presumably, these aggregates were melted from the large $PC_{71}BM$-rich domains owing to penetration of SH-na into the active layer in the dipping process. We note that the simplified 1D in-plane GISAXS profile fitting result reveals mainly the in-plane characteristic lengths of the $PC_{71}BM$ aggregates. 3D structural characterization requires simulation of 2D GISAXS pattern, which is very difficult for the complicated system characterized with the multi-length scales and will be more so for the present cases with dipping or adding additives due to the presence of bimodal size distribution obtained from the in-plane GISAXS profile analysis for the present system. Therefore, we mainly analyze the in-plane GISAXS profiles for all the cases for mainly in-plane dominated structural features.

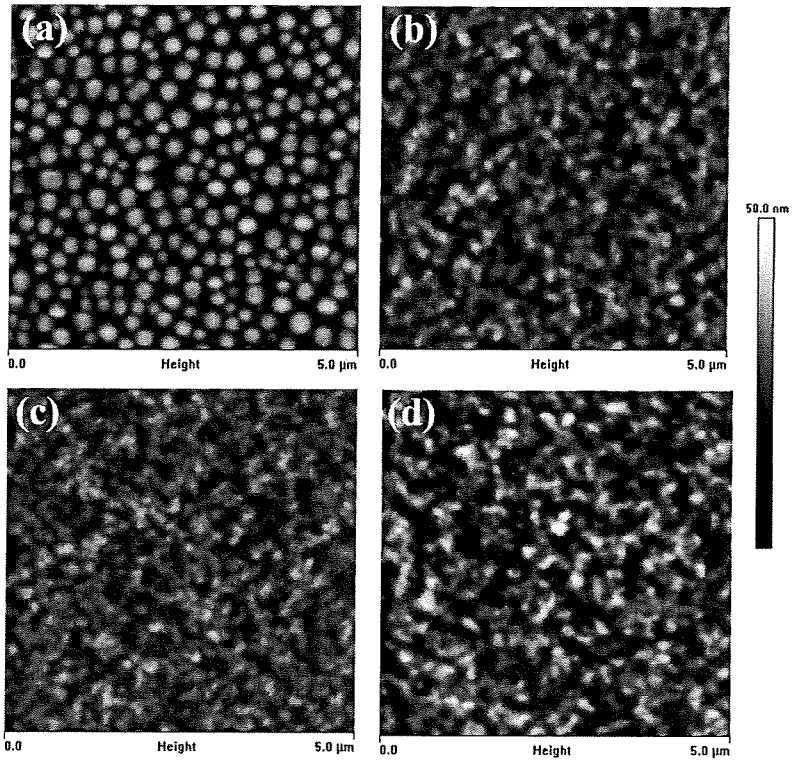


**Figure 5.** AFM height images (5 × 5 $μm^2$) of the PTB7:$PC_{71}BM$ active layers processed; a) without additive, b) with SH-na additive, c) without additive but with the dipping treatment, and d) with SH-na additive followed by the dipping treatment. The corresponding root mean square roughnesses were 6.6, 4.5, 3.8, and 4.8 nm, respectively.

Few GISAXS studies of low band-gap polymer blend PCBM processed with additives reported that PCBM often formed fractal-like aggregations in the active layers.[35] Figure 4d shows the fitted GISAXS profiles for the active layers processed with SH-na additive and that followed by the dipping treatment, which can be best-fitted by the bimodal size distribution (fractal and sphere aggregates models in the Supporting Information) to obtain primary (diameter $2R = 44.6$ or 33.4 nm) and small (diameter $2r = 3.6$ or 4.6 nm) $PC_{71}BM$ aggregates (as shown in


© 2016 WILEY-VCH Verlag GmbH & Co. KGaA, Weinheim

**Table 2.** Structural parameters used in the GISAXS data fitting for the $PC_{71}BM$ aggregates of a bimodal size distribution of the PTB7:$PC_{71}BM$ active layers processed with the different routes indicated. The parameters $2A$ and $2B$ are the major and minor axes of ellipsoidal aggregates, and $2r$ is the diameter of spherical aggregates with the polydispersity $P$ of Schultz distribution; $D_f$ and $\xi_y$ are the fractal dimension and in-plane correlation length of the fractal clusters of the primary aggregates (with the diameter of $2R$). The asteroids mark the insensitive parameters in the data fitting.

| Additive | Dipping | Large Aggregates | | | Small Aggregates | | Aggregate Shape |
|---|---|---|---|---|---|---|---|
| | | $2A$ [nm] | $2B$ [nm] | $P$ [%] | $2r$ [nm] | $P$ [%] | |
| Without | – | 14 ± 6 | 260 ± 26 | 40 | 60 | 42 | Ordered Oblates[a] |
| Without | Yes | 183 ± 80 | 20* | 50 | 10 ± 6 | 35 | Random Prolates |
| Additive | Dipping | Fractal structure | | Primary aggregates in fractal | Small aggregates | | Aggregate Shape |
| | | $D_f$ | $\xi_y$ [nm] | $2R$ [nm] | $P$ [%] | $2r$ [nm] | $P$ [%] | |
| SH-na | – | 2.8 ± 0.1 | 140 | 44.6 ± 3 | 27 | 3.6* | 89 | Spheres[b] |
| SH-na | Yes | 2.5 ± 0.1 | 100 | 33.4 ± 20 | 59 | 4.6 ± 3 | 83 | |
| DIO | – | 2.0 ± 0.1 | 42 ± 2 | 5.4 ± 4 | 48 | – | – | Spheres |

[a]A mean spacing (ordered distance) of 312 nm is fitted for the large aggregates using a structure factor approximated by hard sphere interactions together with the oblate form factor; [b]Large spherical aggregates clustered with a fractal strucutre, coexisted with dispersed small aggregates.

Table 2).[31] These sizes are relatively small compared to the previous cases processed without additive (260 nm) or with solely dipping treatment (183 nm). To account for the steep intensity rise in the low-$q$ region ($q < 0.01$ Å$^{-1}$) (Figure 4d), the large $PC_{71}BM$ aggregates are further modeled to be interconnected for forming fractal-like clusters with the fitted fractal dimension (relevant to the porosity of the clusters) $D_f = 2.8$ or 2.5 and the in-plane correlation length $\xi_y = 140$ or 100 nm (parameters are listed in Table 2) for the active layer with SH-na additive or that further subject to dipping treatment (Figure 4d).[36] After the dipping treatment, the large $PC_{71}BM$ aggregates partially dissolved into smaller aggregates (as suggested by the fitted parameters summarized in Table 2), which would increase the interfaces of PTB7/$PC_{71}BM$ in the active layer for promoted $J_{sc}$ values of the PSCs. In contrast, the GISAXS profile for the active layer processed with DIO additive could be best-fitted (Figure 4d) (fractal aggregates model in the Supporting Information) using finer primary $PC_{71}BM$ aggregates with 5.4 nm diameter that further formed fractal-like clusters with $D_f = 2.0$ and $\xi_y = 42$ nm. Overall, the GISAXS/GIWAXS results suggest that DIO could disperse $PC_{71}BM$ better than SH-na did. Nevertheless, the dual-functional SH-na is superior since it facilitated not only $PC_{71}BM$ dispersion and percolation in multi-length scales but also PTB7 crystallization.

### 2.4. Surface Morphology

Shown in Figure 5a is the AFM image observed for the PTB7:$PC_{71}BM$ active layer processed without additive, exhibiting bright, phase-separated, disk-like domains with polydisperse sizes ≈260 ± 100 nm, a mean domain spacing ≈300–350 nm, and a film surface root-mean-square roughness of 6.6 nm.[14,37] These features are consistent with those of the large $PC_{71}BM$-rich aggregates revealed with the GISAXS result (Table 2). Especially, the large lateral domain size with the AFM surface profile (Figure S9, Supporting Information) corresponds well to the oblate features of the ellipsoid model used in the GISAXS data fitting with $2A = 14$ nm and $2B = 260$ nm. With SH-na additive and/or the dipping treatment, these large discrete $PC_{71}BM$-rich domains could be partially dissolved into smaller and interconnected domains (from oblate- to strip-like aggregates that remain partially interconnected for fractal-like networks) along with reduced surface roughness (3.8–4.8 nm), as shown in Figure 5b,d. These interconnected networks also correspond to the proposed model of fractal aggregates of $PC_{71}BM$ aggregates in the previous GISAXS data analysis. Recently, similar worm-like $PC_{71}BM$ networks were also visualized with film-depth-dependent AFM images.[37]

Further, X-ray photoelectron spectroscopy (XPS) measurements[38] were conducted for these PTB7:$PC_{71}BM$ active layers to determine the surface compositions after dipping treatment. Note that the SH-na in the films is removed by prolong vacuum pump in the vacuum chamber of XPS. The sulfur composition peak in the XPS spectra measured (Figure S10, Supporting Information) can be attributed solely to thiophene-containing PTB7, whereas the carbon composition peak has convoluted contributions from PTB7 and $PC_{71}BM$. After the dipping treatment, the C/S atom ratio (5.46) of the active layer processed with SH-na additive slightly increases to 5.82 (cf. Table S7, Supporting Information), suggesting that surface $PC_{71}BM$ could be hence enriched without enlarging surface roughness (≈4.8 nm).

The dipping-treatment-induced $PC_{71}BM$-rich surface layer was consistently evidenced with neutron reflectivity (NR) of a high sensitivity to the $PC_{71}BM$ distribution in the vertical direction of the film.[39] This is because of a much higher neutron scattering length density (SLD) of fullerenes of $PC_{71}BM$. In contrast, the polymer has a low SLD value due to a high content of hydrogens (of a negative neutron scattering length, as detailed in the Supporting Information).[40] The measured neutron SLD values for the neat $PC_{71}BM$ and PTB7 films are $4.66 \times 10^{-6}$ and $1.17 \times 10^{-6}$ Å$^{-2}$, respectively. Therefore, a high SLD value corresponds to a layer of high $PC_{71}BM$ composition. Figure S11 (Supporting Information) shows the NR data and the correspondingly fitted SLD profiles versus the film depth for the PTB7:$PC_{71}BM$ film processed with SH-na additive and that further subjected to the dipping treatment. For the active layer processed with SH-na additive, the fitted SLD profile using a two-layer model exhibits a relatively uniform


© 2016 WILEY-VCH Verlag GmbH & Co. KGaA, Weinheim

SLD profile with the SLD value $3.02 \times 10^{-6}$ Å$^{-2}$ (0–90 nm) and slightly decreased SLD value $2.92 \times 10^{-6}$ Å$^{-2}$ (90–115 nm), as shown in Figure S11b (Supporting Information). In contrast, the fitted SLD using a three-layer model profile for the dipped treatment exhibits a surface layer (≈20 nm in the overall film thickness about 115 nm, which is near the actual thickness 100 nm of active layer) with high SLD peaked at $4.0 \times 10^{-6}$ Å$^{-2}$ (Figure S11d, Supporting Information), corresponding to a peak $PC_{71}BM$ composition of ≈80% (as estimated based on the respective SLD values of the two components respectively measured).[41] This $PC_{71}BM$-enriched surface layer is followed by a middle sublayer (≈40 nm thickness) of relatively lower SLD and a bottom sublayer (≈55 nm thickness) of slightly enhanced SLD. Presumably, in the dipping process $PC_{71}BM$ diffused from the middle of active layer to the surface, resulting in the slight decrease at the middle of active layer (20–60 nm) and increased at the surface (0–20 nm). The NR result demonstrates that our unique dipping treatment can effectively induce a $PC_{71}$ BM-enriched surface for the active layer that would favor electron collection with the conventional device structure. The fitted SLD profiles, however, reveal slight changes in the thickness of the active layer, presumably induced by the dipping treatment in forming the $PC_{71}BM$-enriched surface.

### 2.5. Correlations of Hole and Electron Mobility to Morphology

Hole-only and electron-only devices were fabricated to reveal the respective hole and electron mobility, and their correlations to the changes of the morphological features observed for the active layers with the different processing routes. Based on the *J–V* curves measured (Figure S12, Supporting Information) and the space-charge-limited-current equation (the Mott–Gurney law) $J = 9\varepsilon\varepsilon_0\mu(V - V_{bi})^2/8L^3$,[42] the hole mobility $\mu_h$ values of $1.95 \times 10^{-4}$, $2.75 \times 10^{-4}$, and $2.03 \times 10^{-4}$ cm$^2$ V$^{-1}$ s$^{-1}$ respectively for the active layers processed with DIO, SH-na, and that without additive but with the dipping treatment. These values are increasingly better than $9.12 \times 10^{-5}$ cm$^2$ V$^{-1}$ s$^{-1}$ obtained for the active layer processed without any additive nor the dipping treatment. We note that this increasing trend of $\mu_h$ correlates well to the increase of the polymer crystallinity observed for these films (cf. GIWAXS in Figure 4a and Table S5 in the Supporting Information). Specifically, the highest $\mu_h$ for the active layer processed with SH-na followed by the dipping treatment corresponds to the highest crystallinity of PTB7 observed.

Moreover, the device processed with DIO additive has relatively finest $PC_{71}BM$ dispersion (cf. Table 2) exhibits a relatively high electron mobility $\mu_e = 1.01 \times 10^{-3}$ cm$^2$ V$^{-1}$ s$^{-1}$ among these films; which is nearly two orders of magnitude higher than that ($5.01 \times 10^{-5}$ cm$^2$ V$^{-1}$ s$^{-1}$) measured for the device processed without additive nor dipping. The active layer processed with SH-na exhibit $\mu_e = 6.46 \times 10^{-4}$ cm$^2$ V$^{-1}$ s$^{-1}$, which can be further improved to $7.41 \times 10^{-4}$ cm$^2$ V$^{-1}$ s$^{-1}$ after the dipping treatment. For the active layer processed without additive but subject to the dipping treatment, an impressive comparable $\mu_e = 7.08 \times 10^{-4}$ cm$^2$ V$^{-1}$ s$^{-1}$ was also obtained. This dramatically improved $\mu_e$ indicates that the novel dipping process with a methanol solution of a critical SH-na concentration (to diffuse an adequate amount of SH-na into the just cast film) could efficiently modify $PC_{71}BM$ dispersion behavior in the active layer for the improved electron mobility observed.

Overall, the charge mobility result suggests that the active layer processed with SH-na followed by the dipping treatment could lead to greatly improved charge mobility of both electron and hole for a relatively balanced electron/hole mobility ratio $R_\mu = \mu_e/\mu_h \approx 2$ among the several processing routes studied, hence the best PCE of 8.75% obtained.[37] In contrast, with the most impressively improved $\mu_e$ but less improved $\mu_h$ for a much less unbalanced $R_\mu$ value of 5.04, the active layer processed with DIO additive resulted in moderately improved PCE of 6.73%. Characterized by the bimodal $PC_{71}BM$ size dispersion with coexisted large and small $PC_{71}BM$ aggregates (Table 2), the active layers processed with SH-na have better enhanced $\mu_h$ and better balanced $R_u$, despite that $\mu_e$ is not best-improved compared to that of the DIO case. In practice, increasingly better PCE values are observed with increasingly balanced charge mobility ratio $R_\mu$ of the SH-na-processed cases as shown in Table 1 and **Table 3**. The correlations between the charge mobility (value and ratio) and morphology outlined above suggest that an optimized device performance needs comparably improved hole and electron mobility. Namely, both high PTB7 crystallinity and fine $PC_{71}BM$ dispersion are required. This makes the morphology control of the PSC a delicate trade-off, since $PC_{71}BM$ cannot disperse alone without penetrating into the polymer phase in the two-phase system. Namely, $PC_{71}BM$ dispersion needs to balance with polymer crystallization, suggesting that the multi-length-scale dispersion of $PC_{71}BM$ observed may be a general feature of fullerene-based high-performance PSCs.[43]

Schematic diagrams in **Figure 6** summarize the observed additive effects with DIO, SH-na, and the dipping treatment, on modulating the morphology of the active layer of PTB7:$PC_{71}BM$. The active layer processed without additive is characterized with large and discrete $PC_{71}BM$-rich domains, leading to relatively less continuous pathways of charge transport and relatively less PTB7/$PC_{71}BM$ interfaces for exciton dissociation (Figure 6a). For the active layer processed with DIO additive, PTB7 and $PC_{71}BM$ are mutually well dispersed in the two-component system, hence more restriction on PTB7 chain packing (or less crystalline domains) (Figure 6b). Processed with SH-na, the active layer has relatively well dispersed

**Table 3.** Hole and electron mobilities, $\mu_h$ and $\mu_e$, and their ratio $R_\mu$ (= $\mu_e/\mu_h$) of the PTB7:$PC_{71}BM$ devices processed with different routes as indicated.

| Additive | Dipping | $\mu_h$ [cm$^2$ V$^{-1}$ s$^{-1}$] | $\mu_e$ [cm$^2$ V$^{-1}$ s$^{-1}$] | $R_\mu$ (= $\mu_e/\mu_h$) |
|---|---|---|---|---|
| Without | – | $9.12 \pm 0.38 \times 10^{-5}$ | $5.01 \pm 0.62 \times 10^{-5}$ | 0.55 |
| DIO | – | $1.95 \pm 0.25 \times 10^{-4}$ | $1.01 \pm 0.42 \times 10^{-3}$ | 5.18 |
| SH-na | – | $2.75 \pm 0.17 \times 10^{-4}$ | $6.46 \pm 0.25 \times 10^{-4}$ | 2.35 |
| Without | Yes | $2.03 \pm 0.41 \times 10^{-4}$ | $7.08 \pm 0.27 \times 10^{-4}$ | 3.48 |
| SH-na | Yes | $3.63 \pm 0.23 \times 10^{-4}$ | $7.41 \pm 0.21 \times 10^{-4}$ | 2.04 |


© 2016 WILEY-VCH Verlag GmbH & Co. KGaA, Weinheim

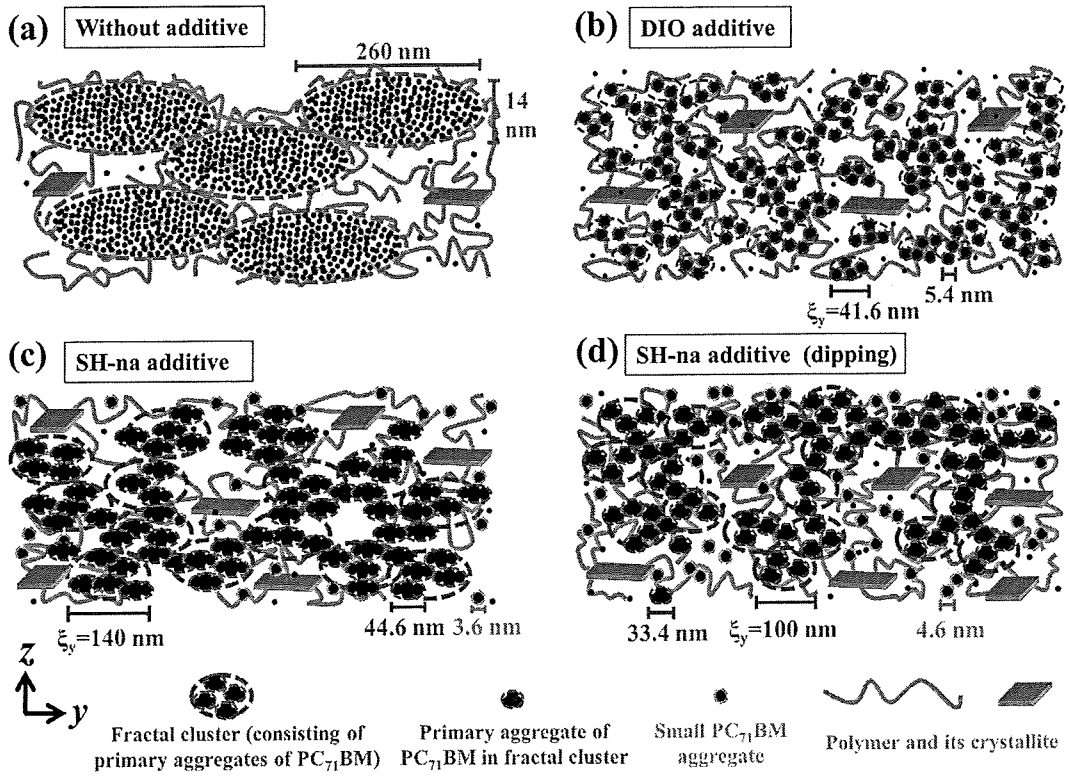


**Figure 6.** Schematic diagrams (cross sections of the active layers) illustrate the feature dispersions of $PC_{71}BM$ and PTB7 crystalline domains in the PTB7:$PC_{71}BM$ active layers processed with the different routes indicated. Note the $PC_{71}BM$-enriched surface layer in panel (d) with the dipping treatment.

$PC_{71}BM$ aggregates in multi-length scales, allowing better growth of the polymer crystalline domains within the fractal $PC_{71}BM$ networks, thereby forming interpenetrating networks of the polymer crystalline domains with $PC_{71}BM$ aggregates in the active layer (Figure 6c). The dipping treatment on the active layer processed with SH-na additive further enriches the film surface with $PC_{71}BM$ (Figure 6d).

## 3. Conclusions

We have proposed a novel processing route with novel SH-na additive for PSCs that can efficiently tailor the bulk and surface morphologies of the active layer of PTB7:$PC_{71}BM$. Through hydrogen bonding with PTB7 and $PC_{71}BM$, SH-na facilitates both PTB7 chain packing and $PC_{71}BM$ dispersion in a multi-length scale for forming $PC_{71}BM$ aggregates with a bimodal size distribution in the active layer. The subsequent dipping treatment in a methanol solution with a critical concentration of SH-na can enrich the active layer surface with $PC_{71}BM$, leading to the best PCE value of 8.75%. The proposed processing with SH-na improves both the electron and hole mobility in delicate balance via trading off slightly the $PC_{71}BM$ dispersion for better PTB7 chain packing for an optimized electron-to-hole mobility ratio close to 2.0. Solvent additive plays a critical role on the morphology control of different extents of polymer crystallinity and $PC_{71}BM$ dispersion. The proposed PSC processing with SH-na and the trade-off concept between polymer crystallization and $PC_{71}BM$ dispersion in morphological controls may be applicable in general PSC morphological optimization.

## 4. Experimental Section

*Device Fabrication*: For device fabrication, ITO glass was cleaned sequentially with detergent aqueous solution, deionized water, acetone, and isopropyl alcohol, followed by treatment with oxygen plasma at a pressure of $1.93 \times 10^{-1}$ torr for 5 min. A layer of PEDOT:PSS (25 nm) (Clevios AI4083, 1.5 wt% in water) was spin-cast on the treated ITO and dried for 10 min at 140 °C. Active layers (about 100 nm) were spin-cast from the blend solutions of PTB7:$PC_{71}BM$ (1:1.5 w/w, 25 mg $mL^{-1}$) with or without 3% additive (DIO or SH-na) onto the PEDOT: PSS layer. The active layers were then selectively dipped into a methanol solution containing SH-na (of optimized 4.5 vol%) for 3 s, followed by spinning off residual solution. For device preparation, a thin Ca layer (5 nm) overlayered with aluminum (100 nm) as the cathode was deposited on the active layer in vacuum thermal evaporator (through a shadow mask) under a vacuum pressure lower than $2 \times 10^{-6}$ torr; the active area of a typical device was about 7.5 $mm^2$. After ITO cleaning and PEDOT:PSS spin-casting, devices were fabricated in a glove box with argon.

*Methodologies*: The thicknesses of the active layers were measured by Tencor P-10 Surface Profiler. UV–Vis and infrared spectra were respectively measured using a Perkin–Elmer (Lambda 19) UV–Vis spectrometer and a Perkin–Elmer spectrum RXI FT-IR system. The current–voltage (*J–V*) curves were measured under atmosphere using a Keithley 2400 source-measure unit and an AM 1.5G solar simulator


© 2016 WILEY-VCH Verlag GmbH & Co. KGaA, Weinheim

(Oriel 94021A, 150 W from Newport). Illumination intensity of 100 mW $cm^{-2}$ irradiation was calibrated using a standard monocrystal Si reference cell (Oriel 91150V from Newport) for accurate light source intensity. The EQE data were measured in ambient environment, based on a system (model QE-R) of Enli Technology Co, with a light source from a filtered 150 W xenon lamp (Oriel, U.S.A.); EQE ($\lambda$) = 12 400 ($J_{sc}/\lambda\phi$) was normalized by the incident radiative flux $\phi$ (mW $cm^{-2}$). GIWAXS/GISAXS were measured at the BL 17A and 23A Endstation of the National Synchrotron Radiation Research Center, Taiwan, as detailed in the Supporting Information.[44] Neutron reflectivity data were measured using the BL16 SOFIA neutron reflectometer in J-PARC/MLF, Japan.[45] AFM topography images were measured by the scanning probe microscopy (Digital Instrument Nanoscope V). XPS spectra were obtained with a photoelectron spectroscopy system (VG, MULTILAB 2000) under a base pressure of $1 \times 10^{-9}$ mbar by using monochromatized Mg (Ka) X-rays ($h\nu$ = 1254.6 eV).

## Supporting Information

Supporting Information is available from the Wiley Online Library or from the author.

## Acknowledgements

The authors thank the Ministry of Education and the Ministry of Science and Technology of the Republic of China for the financial aid through project NSC-101–2120-M-007–004, NSC-102–2633-M-007–002, and NSC 102–2221-E-007–131. The authors thank Tsong-Yuo Yang for the neutron reflectivity data analysis.

Received: December 7, 2015
Revised: January 28, 2016
Published online: March 4, 2016

[1] a) F. C. Krebs, J. Fyenbo, D. M. Tanenbaum, S. A. Gevorgyan, R. Andriessen, B. Remoortere, Y. Galagand, M. Jørgensen, *Energy Environ. Sci.* **2011**, *4*, 4116; b) W. Chen, M. P. Nikiforov, S. B. Darling, *Energy Environ. Sci.* **2012**, *5*, 8045; c) F. Liu, Y. Gu, X. Shen, S. Ferdous, H.-W. Wanga, T. P. Russell, *Prog. Polym. Sci.* **2013**, *38*, 1990; d) D. B. Darling, F. You, *RSC Adv.* **2013**, *3*, 17633.

[2] X. Guo, C. Cui, M. Zhang, L. Huo, Y. Huang, J. Hou, Y. Li, *Energy Environ. Sci.* **2012**, *5*, 7943.

[3] S. H. Liao, Y. L. Li, T. H. Jen, Y. S. Cheng, S. A. Chen, *J. Am. Chem. Soc.* **2012**, *134*, 14271.

[4] L. Lu, T. Xu, W. Chen, J. M. Lee, Z. Luo, I. H. Jung, H. Park, S. O. Kim, L. Yu, *Nano Lett.* **2013**, *13*, 2365.

[5] a) H. Choi, S. J. Ko, Y. Choi, P. Joo, T. Kim, B. R. Lee, J. W. Jung, H. J. Choi, M. Cha, J. R. Jeong, I. W. Hwang, M. H. Song, B. S. Kim, J. Y. Kim, *Nat. Photonics* **2013**, *7*, 732; b) S. W. Baek, J. Noh, C. H. Lee, B. S. Kim, M. K. Seo, J. Y. Lee, *Sci. Rep.* **2013**, *3*, 1726; c) L. Lu, Z. Luo, T. Xu, L. Yu, *Nano Lett.* **2013**, *13*, 59; d) H. Choi, J. P. Lee, S. J. Ko, J. W. Jung, H. Park, S. Yoo, O. Park, J. R. Jeong, S. Park, J. Y. Kim, *Nano Lett.* **2013**, *13*, 2204.

[6] S. H. Liao, H. J. Jhuo, P. N. Yeh, Y. S. Cheng, Y. L. Li, Y. H. Lee, S. Sharma, S.-A. Chen, *Sci. Rep.* **2014**, *4*, 6813.

[7] Y. Liu, J. Zhao, Z. Li, C. Mu, W. Ma, H. Hu, K. Jiang, H. Lin, H. Ade, H. Yan, *Nat. Commun.* **2014**, *5*, 5293.

[8] a) A. Kojima, K. Teshima, Y. Shirai, T. Miyasaka, *J. Am. Chem. Soc.* **2009**, *131*, 6050; b) H. Zhou, Q. Chen, G. Li, S. Luo, T. b. Song, H. S. Duan, Z. Hong, J. You, Y. Liu, Y. Yang, *Science* **2014**, *345*, 542.

[9] a) X. Yang, J. Loos, S. C. Veenstra, W. J. H. Verhees, M. M. Wienk, J. M. Kroon, M. A. J. Michels, R. A. J. Janssen, *Nano Lett.* **2005**, *5*, 579; b) M. Y. Chiu, U. S. Jeng, C. H. Su, K. S. Liang, K. H. Wei, *Adv. Mater.* **2008**, *20*, 2573; c) W. Ma, C. Yang, X. Gong, K. Lee, A. J. Heeger, *Adv. Funct. Mater.* **2005**, *15*, 1617.

[10] a) J. Jo, S. I. Na, S. S. Kim, T. W. Lee, Y. Chung, S. J. Kang, D. Vak, D. Y. Kim, *Adv. Funct. Mater.* **2009**, *19*, 2398; b) Z. He, F. Liu, C. Wang, J. Chen, L. He, D. Nordlund, H. Wu, T. P. Russell, Y. Cao, *Mater. Horiz.* **2015**, *2*, 592.

[11] a) T. Agostinelli, T. A. M. Ferenczi, E. Pires, S. Foster, A. Maurano, C. Muller, A. Ballantyne, M. Hampton, S. Lilliu, M. C. Quiles, H. Azimi, M. Morana, D. D. C. Bradley, J. Durrant, J. E. Macdonald, N. Stingelin, J. Nelson, *J. Polym. Sci., Part B: Polym. Phys.* **2011**, *49*, 717; b) J. T. Rogers, K. Schmidt, M. F. Toney, E. J. Kramer, G. C. Bazan, *Adv. Mater.* **2011**, *23*, 2284.

[12] a) J. K. Lee, W. L. Ma, C. J. Brabec, J. Yuen, J. S. Moon, J. Y. Kim, K. Lee, G. C. Bazan, A. J. Heeger, *J. Am. Chem. Soc.* **2008**, *130*, 3619; b) J. Peet, J. Y. Kim, N. E. Coates, W. L. Ma, D. Moses, A. J. Heeger, G. C. Bazan, *Nat. Mater.* **2007**, *6*, 497.

[13] a) J. Peet, C. Soci, R. C. Coffin, T. Q. Nguyen, A. Mikhailovsky, D. Moses, G. C. Bazan, *Appl. Phys. Lett.* **2006**, *89*, 252105; b) H. Y. Chen, H. Yang, G. Yang, S. Sista, R. Zadoyan, G. Li, Y. Yang, *J. Phys. Chem. C* **2009**, *113*, 7946.

[14] Y. Liang, Z. Xu, J. Xia, S. T. Tsai, Y. Wu, G. Li, C. Ray, L. Yu, *Adv. Mater.* **2010**, *22*, 1.

[15] a) Y. Sun, C. Cui, H. Wang, Y. Li, *Adv. Energy Mater.* **2011**, *1*, 1058.

[16] a) T. K. An, I. Kang, H. J. Yun, H. Cha, J. Hwang, S. Park, J. Kim, Y. J. Kim, D. S. Chung, S. K. Kwon, Y. H. Kim, C. E. Park, *Adv. Mater.* **2013**, *25*, 7003; b) J. S. Moon, C. J. Takacs, S. Cho, R. C. Coffin, H. Kim, G. C. Bazan, A. J. Heeger, *Nano Lett.* **2010**, *10*, 4005; c) J. Jo, A. Pron, P. Berrouard, W. L. Leong, J. D. Yuen, J. S. Moon, M. Leclerc, A. J. Heeger, *Adv. Energy Mater.* **2012**, *2*, 1397; d) Y. Kim, H. R. Yeom, J. Y. Kim, C. Yang, *Energy Environ. Sci.* **2013**, *6*, 1909; e) C. H. Woo, P. M. Beaujuge, T. W. Holcombe, O. P. Lee, J. M. J. Frechet, *J. Am. Chem. Soc.* **2010**, *132*, 15547; f) C. V. Hoven, X. D. Dang, R. C. Coffin, J. Peet, T. Q. Nguyen, G. C. Bazan, *Adv. Mater.* **2010**, *22*, E63.

[17] a) K. S. Chen, H. L. Yip, C. W. Schlenker, D. S. Ginger, A. K. Y. Jen, *Org. Electron.* **2012**, *13*, 2870; b) N. K. Zawack, T. R. Andersen, J. W. Andreasen, L. H. Rossander, H. F. Dam, M. Jørgensen, F. C. Krebs, *J. Mater. Chem. A* **2014**, *2*, 18644.

[18] a) X. Liu, W. Wen, G. C. Bazan, *Adv. Mater.* **2012**, *24*, 4505; b) S. Nam, J. Jang, H. Cha, J. Hwang, T. K. An, S. Park, C. E. Park, *J. Mater. Chem.* **2012**, *22*, 5543.

[19] H. Zhou, Y. Zhang, J. Seifter, S. D. Collins, C. Luo, G. C. Bazan, T. Q. Nguyen, A. J. Heeger, *Adv. Mater.* **2013**, *25*, 1646.

[20] J. Kong, I. W. Hwang, K. Lee, *Adv. Mater.* **2014**, *26*, 6275.

[21] L. Lu, L. Yu, *Adv. Mater.* **2014**, *26*, 4413.

[22] A. Moliton, J. M. Nunzi, *Polym Int.* **2006**, *55*, 583.

[23] M. R. Hammond, R. J. Kline, A. A. Herzing, L. J. Richter, D. S. Germack, H. W. Ro, C. L. Soles, D. A. Fischer, T. Xu, L. Yu, M. F. Toney, D. M. DeLongchamp, *ACS Nano* **2011**, *5*, 8248.

[24] a) K. Matsubayashi, C. Kajimura, H. Shiratori, Y. Kubo, T. Yoshihara, S. Tobita, *Bull. Chem. Soc. Jpn.* **2010**, *83*, 1067; b) D. Patra, M. Ramesh, D. Sahu, H. Padhy, C. W. Chu, K. H. Wei, H. C. Lin, *Polymer* **2012**, *53*, 1219.

[25] L. Ye, Y. Jing, X. Guo, H. Sun, S. Zhang, M. Zhang, L. Huo, J. Hou, *J. Phys. Chem. C* **2013**, *117*, 14920.

[26] S. H. Liao, H. J. Jhuo, Y. S. Cheng, S. A. Chen, *Adv. Mater.* **2013**, *25*, 4766.

[27] Y. He, Y. Li, *Phys. Chem. Chem. Phys.* **2011**, *13*, 1970.

[28] a) P. J. Brown, D. S. Thomas, A. Kohler, J. S. Wilson, J. S. Kim, C. M. Ramsdale, H. Sirringhaus, R. H. Friend, *Phys. Rev. B* **2003**,


© 2016 WILEY-VCH Verlag GmbH & Co. KGaA, Weinheim

*67*, 064203; b) P. Müller-Buschbaum, *Adv. Mater.* **2014**, *26*, 7692; c) A. Hexemer, P. Müller-Buschbaum, *IUCrJ* **2015**, *2*, 106.

[29] B. A. Collins, J. R. Tumbleston, H. Ade, *J. Phys. Chem. Lett.* **2011**, *2*, 3135.

[30] W. R. Wu, U. Jeng, C. J. Su, K. H. Wei, M. S. Su, M. Y. Chiu, C. Y. Chen, W. B. Su, C. H. Su, A. C. Su, *ACS Nano* **2011**, *5*, 6233.

[31] a) M. S. Su, C. Y. Kuo, M. C. Yuan, U. Jeng, C. J. Su, K. H. Wei, *Adv. Mater.* **2011**, *23*, 3315; b) C. M. Liu, Y. W. Su, J. M. Jiang, H. C. Chen, S. W. Lin, C. J. Su, U. Jeng, K. H. Wei, *J. Mater. Chem. A* **2014**, *2*, 20760.

[32] a) Y. S. Sun, S. W. Chien, J. Y. Liou, *Macromolecules* **2010**, *43*, 7250; b) G. Renaud, R. Lazzari, F. Leroy, *Surf. Sci. Rep.* **2009**, *64*, 255; c) T. Erb, U. Zhokhavets, G. Gobsch, S. Raleva, B. Stühn, P. Schilinsky, C. Waldauf, C.-J. Brabec, *Adv. Funct. Mater.* **2005**, *15*, 1193.

[33] G. J. Hedley, A. J. Ward, A. Alekseev, C. T. Howells, E. R. Martins, L. A. Serrano, G. Cooke, A. Ruseckas, D.W. Samuel, *Nat. Commun.* **2013**, *4*, 2867.

[34] E. Y. Sheu, *Phys. Rev. A* **1992**, *45*, 2428.

[35] a) H. C. Liao, C. S. Tsao, Y. T. Shao, S. Y. Chang, Y. C. Huang, C. M. Chuang, T. H. Lin, C. Y. Chen, C. J. Su, U. S. Jeng, Y. F. Chen, W. F. Su, *Energy Environ. Sci.* **2013**, *6*, 1938; b) C. M. Liu, Y. W. Su, J. M. Jiang, H. C. Chen, S. W. Lin, C. J. Su, U. S. Jeng, K. H. Wei, *J. Mater. Chem. A* **2014**, *2*, 20760.

[36] S. H. Chen, J. Teixeira, *Phys. Rev. Lett.* **1986**, *57*, 2583.

[37] D. Wang, F. Liu, N. Yagihashi, M. Nakaya, S. Ferdous, X. Liang, A. Muramatsu, K. Nakajima, T. P. Russell, *Nano Lett.* **2014**, *14*, 5727.

[38] X. Guo, M. Zhang, W. Ma, L. Ye, S. Zhang, S. Liu, H. Ade, F. Huang, J. Hou, *Adv. Mater.* **2014**, *26*, 4043.

[39] a) T. Wang, N. W. Scarratt, H. Yi, A. D. F. Dunbar, A. J. Pearson, D. C. Watters, T. S. Glen, A. C. Brook, J. Kingsley, A. R. Buckley, M. W. A. Skoda, A. M. Donald, R. A. L. Jones, A. Iraqi, D. G. Lidzey, *Adv. Energy Mater.* **2013**, *3*, 505; b) J. W. Kingsley, P. P. Marchisio, H. Yi, A. Iraqi, C. J. Kinane, S. Langridge, R. L. Thompson, A. J. Cadby, A. J. Pearson, D. G. Lidzey, R. A. L. Jones, A. J. Parnell, *Sci. Rep.* **2014**, *4*, 5286.

[40] A. J. Clulow, A. Armin, K. H. Lee, A. K. Pandey, C. Tao, M. Velusamy, M. James, A. Nelson, P. L. Burn, I. R. Gentle, Paul Meredith, *Langmuir* **2014**, *30*, 1410.

[41] H. J. Liu, U. Jeng, N. L. Yamada, A. C. Su, W. R. Wu, C. J. Su, S. J. Lin, K. H. Wei, M. Y. Chiu, *Soft Matter* **2011**, *7*, 9276.

[42] a) C. Melzer, E. J. Koop, V. D. Mihailetchi, P. W. M. Blom, *Adv. Funct. Mater.* **2004**, *14*, 865; b) M. Y. Chiu, U. Jeng, M. S. Su, K. H. Wei, *Macromolecules* **2010**, *43*, 428.

[43] W. Chen, T. Xu, F. He, W. Wang, C. Wang, J. Strzalka, Y. Liu, J. Wen, D. J. Miller, J. Chen, K. Hong, L. Yu, S. B. Darling, *Nano Lett.* **2011**, *11*, 3707.

[44] U. Jeng, C. H. Su, C. J. Su, K. F. Liao, W. T. Chuang, Y. H. Lai, J. W. Chang, Y. J. Chen, Y. S. Huang, M. T. Lee, K. L. Yu, J. M. Lin, D. G. Liu, C. F. Chang, C. Y. Liu, C. H. Chang, K. S. Liang, *J. Appl. Crystallogr.* **2010**, *43*, 110.

[45] N. L. Yamada, N. Torikai, K. Mitamura, H. Sagehashi, S. Sato, H. Seto, T. Sugita, S. Goko, M. Furusaka, T. Oda, M. Hino, T. Fujiwara, H. Takahashi, A. Takahara, *Eur. Phys. J. Plus* **2011**, *126*, 108.


© 2016 WILEY-VCH Verlag GmbH & Co. KGaA, Weinheim